the centres of the magnetic traps for the two spin species along the z axis[6]. Furthermore, the desired behaviour of the Rabi frequency can be achieved by making, with the first Raman laser, two standing waves in the x and y directions that are both polarized perpendicular to the z axis. For the other Raman laser we only require that it produces a travelling wave with a polarization that has a non-zero projection on the z axis, because we want to realize a $\Delta m = 0$ transition in this case. In the above geometry the skyrmion is created exactly in the plane where the detuning vanishes and in the nodes of the first Raman laser. We note that as the distance between these nodes is generally much bigger than the correlation length, we create in this manner a large skyrmion that will start to shrink but ultimately self-stabilizes at a smaller size. Once created, the skyrmion can be easily observed by the usual expansion experiments that have recently also been used to observe vortices[18]. As with vortex rings, we then observe an almost complete depletion of the condensate in a ring around the position of the skyrmion.□

Methods

To calculate the energy of the skyrmion we solve the equation for the density profile that is obtained from minimizing the energy functional in equation (1). We solve this equation numerically for the region outside the core. Inside the core we solve the equation analytically by using the Thomas–Fermi approximation, which amounts to neglecting the gradients of the density profile. Using our ansatz for $\omega(r)$, the texture gradient potential $V(r) = \hbar^2|\nabla\zeta(\mathbf{r})|^2/2m$ reads:

$$V(r) = \frac{\hbar^2}{2m}\frac{32}{\lambda^2}\frac{(r/\lambda)^2[3 + 2(r/\lambda)^4 + 3(r/\lambda)^8]}{[1 + (r/\lambda)^4]^4} \quad (3)$$

For small r/λ this potential can be approximated by a harmonic potential with a characteristic frequency $\omega_0 = \sqrt{96}\hbar^2/2m^2\lambda^4$ and width $l = \lambda/\sqrt{96}$, as shown in the dotted curve in Fig. 3. Specifically, the use of a Thomas–Fermi approximation is justified when the ratio $2Na/l = 2\sqrt{96}Na/\lambda$ is bigger than 1. From Fig. 1, we observe that this ratio equals approximately 1 for $N = 4$ and increases for larger N.

The lifetime of the skyrmion is estimated by calculating the tunnelling rate from the core to the outer region over the barrier $V(r)$. To this end we employ the following WKB (Wentzel, Kramers and Brillouin) expression for the tunnelling rate[19]:

$$\Gamma = \frac{\omega_0}{2\pi}\exp\left[-2\int_{r_1}^{r_2} dr\sqrt{\frac{2m}{\hbar^2}(V(r) - \mu_{\mathrm{core}})}\right] \quad (4)$$

where μ_{core} is the chemical potential of the core atoms. The radial points r_1 and r_2 are the points where $V(r)$ and μ_{core} intersect, as shown in Fig. 3. The chemical potential μ_{core} is calculated by differentiating the total energy of the core with respect to the number of core atoms.

Received 15 November 2000; accepted 20 April 2001.

1. Myatt, C. J., Burt, E. A., Ghrist, R. W., Cornell, E. A. & Wieman, C. E. Production of two overlapping Bose–Einstein condensates by sympathetic cooling. *Phys. Rev. Lett.* **78,** 586–589 (1997).
2. Stamper-Kurn, D. M. *et al.* Optical confinement of a Bose–Einstein condensate. *Phys. Rev. Lett.* **80,** 2027–2030 (1998).
3. Stenger, J. *et al.* Spin domains in ground-state Bose–Einstein condensates. *Nature* **396,** 345–348 (1998).
4. Hall, D. S., Matthews, M. R., Ensher, J. R., Wieman, C. E. & Cornell, E. A. Dynamics of component separation in a binary mixture of Bose–Einstein condensates. *Phys. Rev. Lett.* **81,** 1539–1542 (1998).
5. Stamper-Kurn, D. M. *et al.* Quantum tunneling across spin domains in a Bose condensate. *Phys. Rev. Lett.* **83,** 661–664 (1999).
6. Matthews, M. R. *et al.* Watching a superfluid untwist itself: Recurrence of Rabi oscillations in a Bose–Einstein condensate. *Phys. Rev. Lett.* **83,** 3358–3361 (1999).
7. Matthews, M. R. *et al.* Vortices in a Bose–Einstein condensate. *Phys. Rev. Lett.* **83,** 2498–2501 (1999).
8. Ho, T.-L. Spinor Bose condensates in optical traps. *Phys. Rev. Lett.* **81,** 742–745 (1998).
9. Ohmi, T. & Machida, K. Bose–Einstein condensation with internal degrees of freedom in alkali atom gases. *J. Phys. Soc. Jpn* **67,** 1822–1825 (1998).
10. Law, C. K., Pu, H. & Bigelow, N. B. Quantum spins mixing in spin Bose–Einstein condensates. *Phys. Rev. Lett.* **81,** 5257–5261 (1998).
11. Ho, T.-L. & Yip, S.-K. Fragmented and single condensate ground states of spin-1 Bose gas. *Phys. Rev. Lett.* **84,** 4031–4034 (2000).
12. Yip, S.-K. Internal vortex structure of a trapped spinor Bose–Einstein condensate. *Phys. Rev. Lett.* **83,** 4677–4681 (1999).
13. Williams, J. E. & Holland, M. J. Preparing topological states of a Bose–Einstein condensate. *Nature* **401,** 568–572 (1999).
14. Skyrme, T. H. R. A non-linear field theory. *Proc. R. Soc. Lond. A* **260,** 127–138 (1961).
15. Skyrme, T. H. R. A unified field theory of mesons and baryons. *Nucl. Phys.* **31,** 556–569 (1962).
16. Julienne, P. S., Mies, F. H., Tiesinga, E. & Williams, C. J. Collisional stability of double Bose condensates. *Phys. Rev. Lett.* **78,** 1880–1883 (1997).
17. Côté, R. *et al.* Collective excitations, NMR, and phase transitions in Skyrme crystals. *Phys. Rev. Lett.* **78,** 4825–4828 (1997).
18. Madison, K. W., Chevy, F., Wohlleben, W. & Dalibard, J. Vortex formation in a stirred Bose–Einstein condensate. *Phys. Rev. Lett.* **84,** 806–809 (2000).
19. Stoof, H. T. C. Macroscopic quantum tunneling of a Bose–Einstein condensate. *J. Stat. Phys.* **87,** 1353–1366 (1997).

Acknowledgements

We thank M. Bijlsma for help in the numerical calculations and for helpful remarks. We also thank J. Anglin, G.'t Hooft, D. Olive and J. Smit for useful discussions. This work is supported by the Stichting voor Fundamenteel Onderzoek der Materie (FOM), which is financially supported by the Nederlandse Organisatie voor Wetenschappelijk Onderzoek (NWO).

Correspondence and requests for materials should be addressed to U.A.K. (e-mail: u.alkhawaja@phys.uu.nl).

Interplay of magnetism and high-T_c superconductivity at individual Ni impurity atoms in $Bi_2Sr_2CaCu_2O_{8+\delta}$

E. W. Hudson*†, K. M. Lang*, V. Madhavan*, S. H. Pan*‡, H. Eisaki§‖, S. Uchida§ & J. C. Davis*

* *Department of Physics, University of California, Berkeley, California 94720, USA*
† *National Institute of Standards and Technology, Gaithersburg, Maryland 20899, USA*
‡ *Department of Physics, Boston University, Boston, Massachusetts 02215, USA*
§ *Department of Superconductivity, University of Tokyo, Yayoi, 2-11-16 Bunkyo-ku, Tokyo 113-8656, Japan*
‖ *Department of Applied Physics, Stanford University, Stanford, California, 94205-4060, USA*

Magnetic interactions and magnetic impurities are destructive to superconductivity in conventional superconductors[1]. By contrast, in some unconventional macroscopic quantum systems (such as superfluid ^{3}He and superconducting UGe_2), the superconductivity (or superfluidity) is actually mediated by magnetic interactions. A magnetic mechanism has also been proposed for high-temperature superconductivity[2–6]. Within this context, the fact that magnetic Ni impurity atoms have a weaker effect on superconductivity than non-magnetic Zn atoms in the high-T_c superconductors has been put forward as evidence supporting a magnetic mechanism[5,6]. Here we use scanning tunnelling microscopy to determine directly the influence of individual Ni atoms on the local electronic structure of $Bi_2Sr_2CaCu_2O_{8+\delta}$. At each Ni site we observe two d-wave impurity states[7,8] of apparently opposite spin polarization, whose existence indicates that Ni retains a magnetic moment in the superconducting state. However, analysis of the impurity-state energies shows that quasiparticle scattering at Ni is predominantly non-magnetic. Furthermore, we show that the superconducting energy gap and correlations are unimpaired at Ni. This is in strong contrast to the effects of non-magnetic Zn impurities, which locally destroy superconductivity[9]. These results are consistent with predictions for impurity atom phenomena[5,6] derived from a magnetic mechanism.

In our studies we use two different $Bi_2Sr_2Ca(Cu_{1-x}Ni_x)_2O_{8+\delta}$ (BSCCO) single crystals, grown by the floating-zone technique. These crystals have $x = 0.005$ with $T_c = 83$ K and $x = 0.002$ with $T_c = 85$ K, respectively. The Ni atoms substitute for Cu atoms in the superconducting CuO_2 plane and are believed to be in the $Ni^{2+}3d^8$ electronic state, as compared to the $Cu^{2+}3d^9$ of Cu. Above the superconducting transition temperature T_c each Ni atom possesses a strong magnetic moment of around $1.5\mu_B$ (ref. 10). The samples

are cleaved in cryogenic ultra-high vacuum at 4.2 K to expose the BiO crystal plane and, when inserted into the scanning tunnelling microscope (STM) head, are imaged with atomic resolution.

For d-wave superconductors, theory predicts that quasi-particle scattering at an impurity atom creates a local electronic state (impurity state) nearby[7,8,11–17]. Such states, which have been analysed for both potential (non-magnetic)[7,8,11,12,14–16] and magnetic[8,12–17] scattering, can be thought of as almost localized quantum orbitals of well defined energy Ω and spatial structure[9,18].

The spatial distribution of impurity states as Ni impurity atoms can be imaged by measuring, as a function of position, the differential tunnelling conductance $G = \mathrm{d}I/\mathrm{d}V$. This is proportional to the local density of states (LDOS) and we refer to this process as LDOS mapping. As an example, Fig. 1 shows two simultaneously acquired LDOS maps taken at sample bias $V = \pm 9$ mV. They reveal both the particle-like (positive bias) and hole-like (negative bias) components of one of the impurity states that exist at each Ni. At +9 mV '+-shaped' regions of higher LDOS are observed, whereas at −9 mV the corresponding higher LDOS regions are 'X-shaped'. LDOS maps at $V = \pm 19$ mV show the particle-like and hole-like components of a second impurity state at Ni whose spatial structure is very similar to that at $V = \pm 9$ mV.

High-resolution ±9-mV LDOS maps (Fig. 2a, b) acquired simultaneously with a topographic image of the BiO surface (Fig. 2c) show in detail how an impurity state consists of two spatially complementary components. By this we mean that the particle-like LDOS is high in regions where the hole-like LDOS is low, and vice versa. To illustrate these relationships, Fig. 2d shows a schematic diagram of the relative locations of Cu atoms, the orientation of the $d_{x^2-y^2}$ superconducting order parameter (OP), and the location of the particle-like (green) and hole-like (purple) components of the impurity state.

We also probe the energy dependence of the LDOS at several

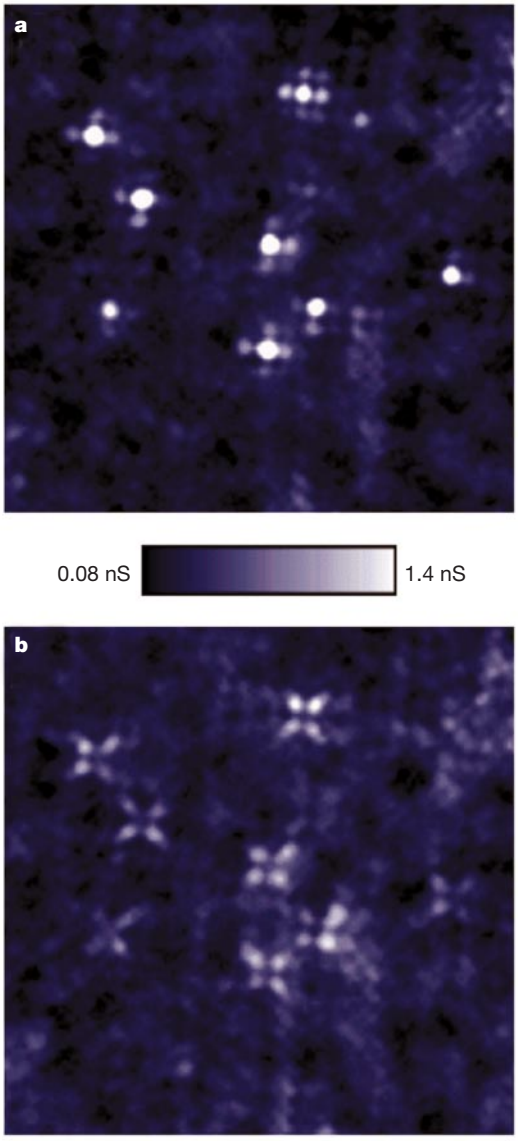

Figure 1 Maps of the local density of electronic states at energies $E = \pm 9$ meV, revealing the locations of the Ni impurity states. Two 128 Å square differential conductance maps of Ni-doped BSCCO. **a**, At sample bias +9 mV, showing the '+-shaped' regions of high local density of states (LDOS) associated with the Ni atoms. **b**, At −9 mV, showing the 45° spatially rotated 'X-shaped' pattern. The differential conductance $G(V) = \mathrm{d}I/\mathrm{d}V$ measured at sample bias voltage V and tunnelling current I is proportional to the LDOS at energy $E = eV$. In such an LDOS map, states associated with positive sample bias are referred to as particle-like whereas those at negative sample bias are hole-like. There are ~8 Ni atom sites in the field of view. As the areal densities of these phenomena in two crystals agree with the two different Ni dopant densities, we conclude that they are associated with Ni atoms. The junction resistance was 1 GΩ at −100 mV for the simultaneously obtained maps and all data were acquired at 4.2 K.

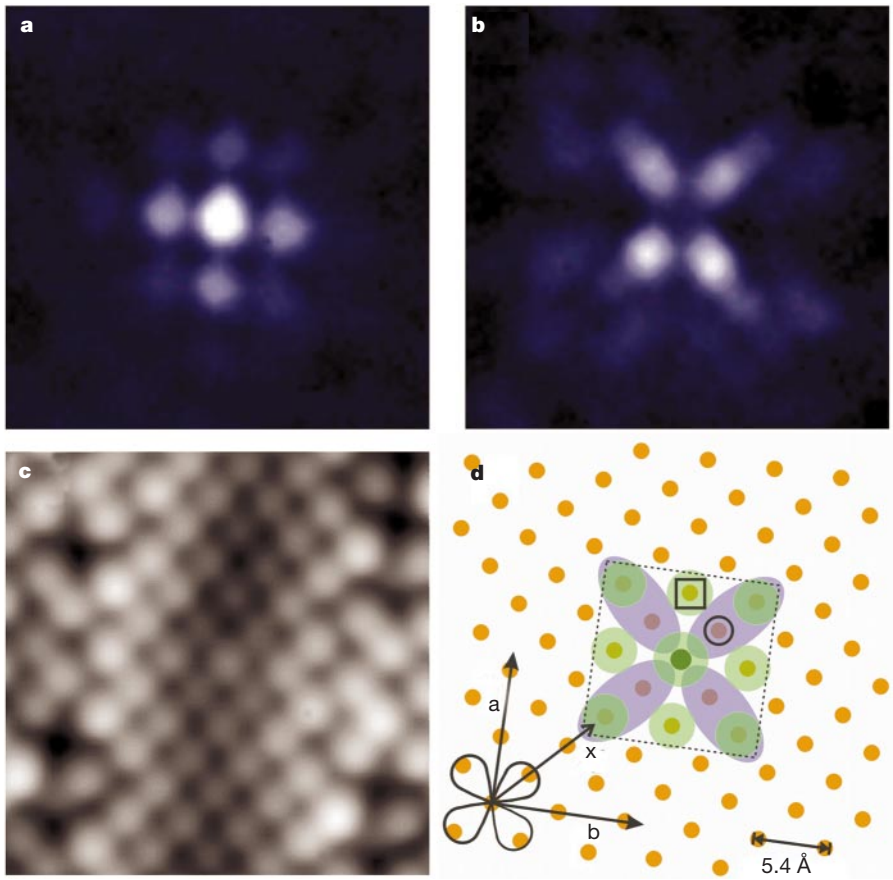

Figure 2 Detailed spatial structure of the impurity state at a single Ni atom. **a**, **b**, 35 Å square differential conductance maps above an Ni atom at (**a**) +9 mV and (**b**) −9 mV. **c**, A 35 Å square atomic resolution topograph of the BiO surface obtained simultaneously with the maps. **d**, Using the information in **a**, **b** and **c** and the fact that the Cu atoms in the CuO_2 plane lie directly beneath the Bi atoms in the BiO plane, we draw a schematic showing the relative position of the Ni atom (black solid circle) with respect to the Cu atoms (orange solid circles) in the invisible CuO_2 plane. Also depicted is the orientation of the $d_{x^2-y^2}$ order parameter with respect to the **a**- and **b**- axis, and the positions of the first NN (open circle) and second NN (open square) atoms where the spectra shown in Fig. 3 are acquired. The ~16 Å square region inside which the spatial integration of the whole impurity-state LDOS was carried out is also shown. The junction resistance is 1 GΩ at −100 mV for all data. The bright central maximum of the '+-shaped' LDOS map always occurs at the site of a Bi surface atom, consistent with the Ni atom being at the Cu site ~5 Å below. The spatial structure in LDOS of an impurity state, when observed at the BiO plane, may not be identical to that in the CuO_2 plane[16]. However, the magnitude of the impurity-state energies should be independent of interlayer matrix element effects.

locations near a Ni atom. Figure 3a shows typical dI/dV spectra taken at four locations: above the Ni atom, above the first nearest neighbour (1-NN) Cu atom, above the second nearest neighbour (2-NN) Cu atom, and at a distance of 30 Å from the impurity site; and Fig. 3b shows the average spectrum for the whole impurity-state region. There are two clear particle-like LDOS peaks above the Ni site. The average magnitudes of these on-site impurity-state energies measured at eight different Ni sites are $\Omega_1 = 9.2 \pm 1.1$ meV and $\Omega_2 = 18.6 \pm 0.7$ meV. Both these peaks become hole-like at all the 1-NN Cu sites and again particle-like at the 2-NN Cu sites. Despite these complexities, the spatially averaged spectrum for this whole region (Fig. 3b) remains very close to particle–hole symmetric.

Several conclusions can be drawn from these data. First, the two on-site LDOS peaks reveal that there are two distinct impurity states associated with each Ni atom. This can be explained by theories that consider both potential and magnetic interactions[8]. In a d-wave superconductor, theory indicates that potential scattering generates a single spin-degenerate impurity state[7,8,11]. A weak additional magnetic interaction between an impurity moment and the quasi-particle spin lifts the spin degeneracy, creating two spin-polarized impurity states at each magnetic impurity atom[8]. The good qualitative agreement between the data and this model indicates that Ni atoms do possess a magnetic moment in the superconducting state.

Second, as shown in Figs 2 and 3, the spectral weight of an impurity state oscillates between particle-like and hole-like as a function of distance from the Ni atom. Nevertheless, the average conductance spectrum over the whole impurity state remains almost particle–hole symmetric. Theoretically, such overall particle–hole symmetry in an impurity-state spectrum is expected when superconductivity is not disrupted[12,14–16,19,20]. Furthermore, calculations for the d-wave impurity-state wavefunction show that the particle-like and hole-like LDOS should be spatially complementary[8,12,14–16]. The agreement of our observations with these theoretical models shows that superconductivity is not disrupted locally by the magnetic moment of Ni.

A third observation is that the superconducting gap magnitude (as deduced from the energy of the coherence peaks) does not change as we approach the impurity site. This is shown in Fig. 4, which shows a series of conductance spectra as a function of distance from the Ni site. The particle-like coherence peak is depleted to provide spectral density for the impurity state, but the gap magnitude (28 mV) deduced from the hole-like coherence peak location is unperturbed.

In summary, two local states in excellent qualitative agreement with d-wave impurity scattering theory can be identified at each Ni impurity atom. The presence of two impurity states indicates that the Ni atom possesses a magnetic moment, whereas the existence

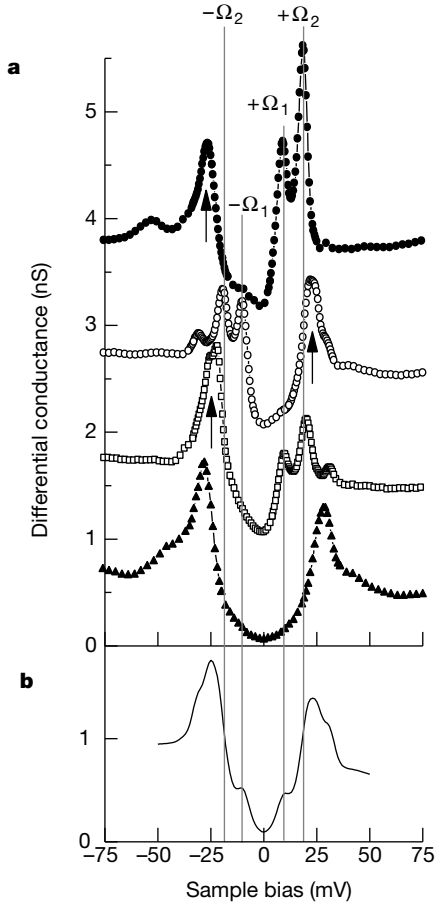

Figure 3 Differential conductance spectra above the Ni atom and at several nearby locations. Differential conductance spectra obtained at four positions near the Ni atom showing the maxima at $V = \pm \Omega_1/e$ and $V = \pm \Omega_2/e$ and the superconducting coherence peaks. These curves are shifted from each other by 1 nS for clarity. **a**, The spectrum above the Ni atom site (solid circles), above the first nearest neighbour Cu atom position (open circles), above the second nearest neighbour Cu atom (squares), and a typical spectrum 30 Å from an impurity atom (triangles). The location of the Ni atom and the first and second nearest neighbours is shown in Fig. 2. The spectra show rapid variations in LDOS magnitude as a function of position. They also reveal the persistence of the coherence peak (shown by the upward pointing arrows) in any given spectrum on the side opposite to the impurity-state resonance peaks. **b**, The average conductance spectrum for a ~16 Å square area centred on an Ni atom, showing the particle–hole symmetric nature of the spatially integrated LDOS. The junction resistance was 1 GΩ at –200 mV for all spectra.

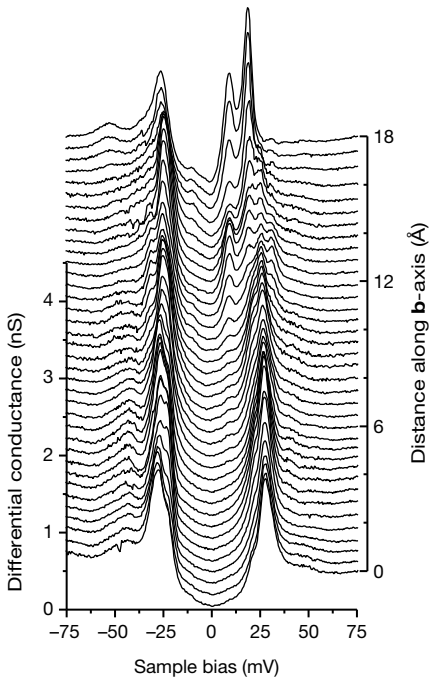

Figure 4 Evolution of the d*I*/d*V* spectra and superconducting energy gap as a function of distance from the Ni atom. A series of differential conductance spectra (shifted vertically from each other for clarity), taken as a function of distance away from the centre of a Ni impurity state along the **b**-axis. The top spectrum is taken above the Ni site. The spectra, each separated by 0.5 Å, show that over a ~20 Å range the magnitude of the superconducting gap $\Delta_0 = 28$ meV, as measured by the separation between the hole-like coherence peak and the Fermi level, is not suppressed in the presence of the Ni impurity. Line cuts approaching the Ni site from other directions lead to the same conclusion. There are variations in Δ_0 throughout the crystal but this study was carried out in a patch with constant Δ_0 of 28 meV. The junction resistance was 1 GΩ at –100 mV for all spectra.

and structure of the particle-like to hole-like oscillations and the constant gap magnitude indicate that superconductivity is nowhere disrupted.

We now turn to the implications of these data for proposals[5,6] that differences between the influence of 'magnetic' Ni and 'non-magnetic' Zn impurity atoms are evidence of a magnetic mechanism for high-temperature superconductivity (HTSC). Previous experimental studies using Ni and Zn impurities have revealed two apparently contradictory aspects of their effects on HTSC. On one hand, resistivity[21,22], microwave surface resistivity[23] and T_c (refs 21, 22) measurements show similar dependences on Zn and Ni doping densities. On the other hand, probes sensitive to magnetic phenomena such as NMR[24–30] and inelastic neutron scattering (INS)[31], and probes of the superfluid density such as penetration depth[23] and muon-spin-rotation (μSR)[32], show marked differences between Ni- and Zn-doped samples.

Analysis of the Ni impurity-state energies using the model of ref. 8 is the first step towards understanding this situation. In that model, potential scattering is represented by an on-site energy U, and magnetic interaction is modelled as having energy $W = J\mathbf{S}\cdot\mathbf{s}$. Here $\mathbf{S}$ is the classical spin of the impurity atom, $\mathbf{s}$ is the quasiparticle spin and J is the exchange energy. The solution for the on-site resonance energy can be written approximately as[8]

$$\frac{\Omega_{1,2}}{\Delta_0} = \frac{-1}{2N_F(U \pm W)\ln|(8N_F(U \pm W))|}$$

Here Δ_0 is the maximum magnitude of the superconducting gap and N_F is the normal density of states per site at the Fermi energy. By substituting the measured values of Ω_1 and Ω_2 and $\Delta_0 = 28$ meV into this equation, we find $N_F U = -0.67$ and $|N_F W| = 0.14$. This represents a surprising new insight because Ni is usually regarded as a source of magnetic scattering, but here we identify the dominant effects as due to potential scattering.

The apparent conflicts between results from different probes may now be reconciled. The first set of probes is sensitive to scattering. Calculation of the potential scattering phase shift $\delta_0 = \tan^{-1}(\pi N_F U)$ for Ni gives $\delta_0 = 0.36\pi$, whereas our previous results showed that Zn is a unitary scatterer ($\delta_0 \approx \pi/2$)[9]. The similarity of these phase shifts imply that phenomena dependent on scattering should be quite similar in Ni- and Zn-doped samples. In fact, using these parameters in an Abrikosov–Gorkov model[1] (and ignoring Ni's magnetic potential), we calculate that T_c would be suppressed only about 20% faster by Zn than by Ni, certainly within the range of experimental observations[21,22].

Among the second set of measurement techniques are those sensitive to superconductivity itself. For example, penetration depth[23] and μSR[32] measurements show that, in the bulk, Zn strongly depletes superfluid density but Ni has a much weaker impact. The STM data now provide a microscopic explanation for these differ-

ences—Zn atoms locally destroy superconductivity[9] while Ni atoms do not.

Finally, magnetic probes sensitive to spin fluctuations reveal marked changes with Zn-doping[24,26–31] but only weak perturbations with Ni-doping[24,25,29,31]. Explanations for these phenomena have been proposed[5,6,27,28,30] whereby Zn behaves like a 'magnetic hole' (a spinless site in an environment of strongly exchange-coupled spins) that strongly alters NN exchange correlations and disrupts superconductivity, whereas Ni retains a magnetic moment that barely perturbs the antiferromagnetic exchange correlations that facilitate superconductivity. Although the NMR and INS data[24–31] are quite consistent with the magnetic component of such models, their predictions for local electronic phenomena at Ni and Zn can only now be tested for the first time. The STM data show that, despite their magnetic moments, scattering at Ni atoms is dominated by potential interactions. Furthermore, whereas Zn atoms locally destroy superconductivity within a 15 Å radius[9], the magnetic Ni atoms coexist with unweakened superconductivity. All these phenomena are consistent with the above proposals.

The resilience of cuprate-oxide high-T_c superconductivity against what should be the destructive effects of a magnetic impurity atom, and its concomitant vulnerability to destruction by a 'magnetic hole', are remarkable. These atomic-scale phenomena are now (through a combination of NMR, μSR and STM) coming into much clearer focus. They point towards a new approach to studying HTSC in which microscopic theories can be tested against an atomically resolved knowledge of impurity-state phenomena. □

Received 8 January; accepted 3 April 2001.

1. Abrikosov, A. A. & Gorkov, L. P. Contribution to the theory of superconducting alloys with paramagnetic impurities. *Sov. Phys. JETP* **12,** 1243–1253 (1961).
2. Monthoux, P., Balatsky, A. V. & Pines, D. Weak-coupling theory of high-temperature superconductivity in the antiferromagnetically correlated copper oxides. *Phys. Rev. B* **46,** 14803–14817 (1992).
3. Moriya, T., Takehashi, Y. & Ueda, K. Antiferromagnetic spin fluctuations and superconductivity in two-dimensional metals—a possible model for high T_C oxides. *J. Phys. Soc. Jpn* **59,** 2905–2915 (1990).
4. Bickers, N. E., Scalapino, D. J. & White, S. R. Conserving approximations for strongly correlated electron systems: Bethe-Salpeter equation and dynamics for the two-dimensional Hubbard model. *Phys. Rev. Lett.* **62,** 961–964 (1989).
5. Monthoux, P. & Pines, D. Spin-fluctuation-induced superconductivity and normal-state properties of $YBa_2Cu_3O_7$. *Phys. Rev. B* **49,** 4261–4278 (1994).
6. Pines, D. Understanding high temperature superconductors: progress and prospects. *Physica C* **282–287,** 273–278 (1997).
7. Balatsky, A. V., Salkola, M. I. & Rosengren, A. Impurity-induced virtual bound states in d-wave superconductors. *Phys. Rev. B* **51,** 15547–15551 (1995).
8. Salkola, M. I., Balatsky, A. V. & Schrieffer, J. R. Spectral properties of quasiparticle excitations induced by magnetic moments in superconductors. *Phys. Rev. B* **55,** 12648–12661 (1997).
9. Pan, S. H. *et al.* Imaging the effects of individual zinc impurity atoms on superconductivity in $Bi_2Sr_2CaCu_2O_{8+\delta}$. *Nature* **403,** 746–750 (2000).
10. Mendels, P. *et al.* Macroscopic magnetic properties of Ni and Zn substituted $YBa_2Cu_3O_x$. *Physica C* **235/240,** 1595–1596 (1994).
11. Salkola, M. I., Balatsky, A. V. & Scalapino, D. J. Theory of scanning tunneling microscopy probe of impurity states in a d-wave superconductor. *Phys. Rev. Lett.* **77,** 1841–1844 (1996).
12. Flatté, M. E. & Byers, J. M. Impurity effects on quasiparticle c-axis planar tunneling and STM spectra in high-Tc cuprates. *Phys. Rev. Lett.* **80,** 4546–4549 (1998).
13. Tsuchiura, H., Tanaka, Y., Ogata, M. & Kashiwaya, S. Local density of states around a magnetic impurity in high-T_C superconductors based on the t-J model. *Phys. Rev. Lett.* **84,** 3165–3168 (2000).
14. Flatté, M. E. Quasiparticle resonant states as a probe of short-range electronic structure and Andreév coherence. *Phys. Rev. B* **61,** R14920–14923 (2000).
15. Haas, S. & Maki, K. Quasiparticle bound states around impurities in $d_{x^2-y^2}$-wave superconductors. *Phys. Rev. Lett.* **85,** 2172–2175 (2000).
16. Martin, I., Balatsky, A. V. & Zaanen, J. Impurity states and interlayer tunneling in high temperature superconductors. Preprint cond-mat/0012446 at <xxx.lanl.gov> (2000).
17. Zhang, G.-M., Hu, H. & Yu, L. Marginal Fermi liquid resonance induced by quantum magnetic impurity in d-wave superconductors. *Phys. Rev. Lett.* **86,** 704–707 (2001).
18. Yazdani, A., Howald, C. M., Lutz, C. P., Kapitulnik, A. & Eigler, D. M. Impurity-induced bound excitations on the surface of $Bi_2Sr_2CaCu_2O_8$. *Phys. Rev. Lett.* **83,** 176–179 (1999).
19. Yazdani, A., Jones, B. A., Lutz, C. P., Crommie, M. F. & Eigler, D. M. Probing the local effects of magnetic impurities on superconductivity. *Science* **275,** 1767–1770 (1997).
20. Flatté, M. E. & Byers, J. M. Local electronic structure of a single magnetic impurity in a superconductor. *Phys. Rev. Lett.* **78,** 3761–3764 (1997).
21. Maeda, A., Yabe, T., Takebayashi, S., Hase, M. & Uchinokura, K. Substitution of 3d metals for Cu in $Bi_2(Sr_{0.6}Ca_{0.4})_3Cu_2O_y$. *Phys. Rev. B* **41,** 4112–4117 (1990).
22. Kuo, Y. K. *et al.* Effect of magnetic and nonmagnetic impurities (Ni,Zn) substitution for Cu in $Bi_2(SrCa)_{2+n}(Cu_{1-x}M_x)_{1+n}O_y$ whiskers. *Phys. Rev. B* **56,** 6201–6206 (1997).
23. Bonn, D. A. *et al.* Comparison of the influence of Ni and Zn impurities on the electromagnetic properties of $YBa_2Cu_3O_{6.95}$. *Phys. Rev. B* **50,** 4051–4063 (1994).
24. Ishida, K. *et al.* Cu NMR and NQR studies of impurities-doped $YBa_2(Cu_{1-x}M_x)_3O_7$ (M=Zn and Ni). *J. Phys. Soc. Jpn* **62,** 2803–2818 (1993).
25. Tokunaga, Y., Ishida, K., Kitaoka, Y. & Asayama, K. Novel relation between spin-fluctuation and superconductivity in Ni substituted high-T_C cuprate $YBa_2Cu_3O_7$: Cu NQR study. *Solid State Comm.* **103,** 43–47 (1997).
26. Mahajan, A. V., Alloul, H., Collin, G. & Marucco, J. F. ^{89}Y NMR probe of Zn induced local moments in $YBa_2(Cu_{1-y}Zn_y)_3O_{6+x}$. *Phys. Rev. Lett.* **72,** 3100–3103 (1994).
27. Bobroff, J. *et al.* Spinless impurities in high-T_C cuprates: Kondo-like behavior. *Phys. Rev. Lett.* **83,** 4381–4384 (1999).
28. Bobroff, J. *et al.* Persistence of Li induced Kondo moments in the superconducting state of cuprates. *Phys. Rev. Lett.* **86,** 4116–4119 (2001).
29. Williams, G. V. M., Tallon, J. L. & Dupree, R. NMR study of magnetic and non-magnetic impurities in $YBa_2Cu_4O_8$. *Phys. Rev. B* **61,** 4319–4325 (2000).
30. Julien, M.-H. *et al.* ^{63}Cu NMR evidence for enhanced antiferromagnetic correlations around Zn impurities in $YBa_2Cu_3O_{6.7}$. *Phys. Rev. Lett.* **84,** 3422–3425 (2000).
31. Sidis, Y. *et al.* Quantum impurities and the neutron resonance peak in $YBa_2Cu_3O_7$: Ni versus Zn. *Phys. Rev. Lett.* **84,** 5900–5903 (2000).
32. Bernhard, C. *et al.* Suppression of the superconducting condensate in the high-T_C cuprates by Zn substitution and overdoping: Evidence for an unconventional pairing state. *Phys. Rev. Lett.* **77,** 2304–2307 (1996).

Acknowledgements

We acknowledge H. Alloul, P. W. Anderson, A. V. Balatsky, D. Bonn, M. Flatté, M. Franz, D.-H. Lee, K. Maki, I. Martin, P. Monthoux, A. Mourachkine, D. Pines, D. Rokhsar, S. Sachdev, D. J. Scalapino and A. Yazdani for conversations and communications, and J. E. Hoffman for help with data analysis. Support was from the Office of Naval Research, the Department of Energy through an LDRD from LBNL, the UCDRD Program, Grant-in-Aid for Scientific Research on Priority Area (Japan), a COE Grant from the Ministry of Education, Japan, the Miller Inst. for Basic Research (J.C.D.), and by the IBM Graduate Fellowship Program (K.M.L.).

Correspondence and requests for materials should be addressed to J.C.D. (e-mail: jcdavis@physics.berkeley.edu).

Liquid marbles

Pascale Aussillous & David Quéré

Laboratoire de Physique de la Matière Condensée, URA 792 du CNRS, Collège de France, 75231 Paris Cedex 05, France

The transport of a small amount of liquid on a solid is not a simple process, owing to the nature of the contact between the two phases. Setting a liquid droplet in motion requires non-negligible forces (because the contact-angle hysteresis generates a force opposing the motion[1]), and often results in the deposition of liquid behind the drop. Different methods of levitation—electrostatic, electromagnetic, acoustic[2], or even simpler aerodynamic[2,3] techniques—have been proposed to avoid this wetting problem, but all have proved to be rather cumbersome. Here we propose a simple alternative, which consists of encapsulating an aqueous liquid droplet with a hydrophobic powder. The resulting 'liquid marbles' are found to behave like a soft solid, and show dramatically reduced adhesion to a solid surface. As a result, motion can be generated using gravitational, electrical and magnetic fields. Moreover, because the viscous friction associated with motion is very small[4], we can achieve quick displacements of the droplets without any leaks. All of these features are of potential benefit in microfluidic applications, and also permit the study of a drop in a non-wetting situation—an issue of renewed interest following the recent achievement of super-hydrophobic substrates[5].

Liquid marbles are obtained by making a small amount of liquid (typically between 1 and 10 mm^3) roll in a very hydrophobic powder (we used lycopodium grains of typical size 20 μm covered with fluorinated silanes). The grains spontaneously coat the drop, which can eventually be transferred onto other substrates. Figure 1 shows a marble of radius 1 mm, made of water and put on a glass plate (which would be wetted by water), where it is observed to adopt a spherical shape. Thanks to the monolayer of grains at the liquid–air interface, the wetting between the glass and the water is suppressed.